ISSN 0036-0295, Russian Metallurgy (Metally), Vol. 2024, No. 5, pp. 1056–1063. © Pleiades Publishing, Ltd., 2024.
Russian Text © The Author(s), 2024, published in Deformatsiya i Razrushenie Materialov, 2024, No. 6, pp. 2–10.

Stress–Strain State of a High-Speed Steel Surface Layer at Plasma Surfacing

S. A. Nevskii[a], *, L. P. Bashenko[a], V. E. Gromov[a], and A. D. Filyakov[a]

[a] *Siberian State Industrial University, Novokuznetsk, 654006 Russia*

**e-mail: nevsky.sergei@yandex.ru*

Received February 22, 2024; revised February 22, 2024; accepted February 29, 2024

Abstract—Using the finite-element method, the problem of thermoelastic stress distribution in a high-speed R2M19 steel coating on a 30KhGSA steel substrate has been solved. Stress distributions in the coating versus distance from the surface have been obtained. It has been found that normal component σ_{yy} of the stress tensor varies nonmonotonically along the rounding radius and monotonically along the central axis. It has also been shown that the von Mises stress intensity rises toward the coating boundary, as a result of which a minimum appears in the dependence of the microhardness on distance to the coating boundary. Stability analysis of carbide phase inclusions subjected to thermoelastic stresses has been carried out. It has turned out that inclusions 10 μm or greater in size are unstable if their thickness is about 1 μm or less.

Keywords: high-speed steel, stress, strain, thermoelasticity

DOI: 10.1134/S003602952470201X

1. INTRODUCTION

Today, techniques for applying wear-resistant high-speed steel coatings by means of highly concentrated energy fluxes are gaining ground. Coatings are deposited using lasers [1], electron beams [2], plasmas [3], etc. These methods provide small fusion penetration and a narrow zone of thermal effect in the substrate. In the case of laser surfacing, however, the probability of hot cracking rises significantly notwithstanding micro- and nanostructuring and high crystallization rate. Electron-beam surfacing requires high vacuum, which limits its applicability to large parts, although it is expected that vacuum-free technologies being developed will remove this restriction.

The plasma method does not experience size and shape limitations, but it results in cold cracking [5], which can be avoided by applying additional thermal treatment. Therefore, the search for conditions for plasma surfacing of high-carbon high-speed steel layers that could prevent cracking and at the same time ensure high mechanical and tribological properties without additional thermal treatments is growing more urgent [6]. To solve this problem, it is insufficient to know only the mechanisms of micro- and nanostructuring during surfacing. It is also necessary to have an idea of stress distribution in the coating and at the coating–substrate interface at different instants of time after the plasma action.

Stresses are usually calculated using methods from the theory of elasticity of inhomogeneous media [7]. These methods are conditionally subdivided into three groups: analytical methods, numerical methods, and analytical–numerical ones. Analytical methods take into consideration the relative thickness of coating. This allows asymptotic expansions to be applied [8, 9]. A disadvantage of such an approach is that there arises the necessity for solving integral equations. In this case, the resulting distributions of stress normal and tangential components are most frequently of a qualitative e character. In analytical approaches emphasis is given to calculating the width and depth of the counterface contact.

In [10, 11], a matrix algorithm approach was suggested as an alternative. Its essence is that conditions at the layer interfaces are coupled through transfer matrices. After a transfer matrix is constructed, stresses and displacements in the first later are calculated by the coupling formula

$$f_1 = \left(\prod_{i=1}^{n} G_1\right) f_n.$$

Here, f_1 is the column vector of the first layer, f_n is the column vector of the nth layer, and G_i is the interlayer transfer matrix. The column vector of each layer includes stresses and displacements in the first layer [10].

However, if the number of layers is large, the matrix becomes cumbersome. Notwithstanding this disadvantage matrix algorithms are successfully applied to solve problems of wave propagation in inhomogeneous layered media [11].

Intensive development of information technologies has given rise to program suites based on finite-element methods [12, 13]. One must adapt these suites to still outstanding problems and provide a deeper insight into coating–substrate contact interaction to select an appropriate grid for adequately splitting the system into elements. Among the advantages of these methods are the feasibility of studying 3D problems, the possibility of inelastic element introduction, and a greater clarity compared with analytical methods.

Unlike the above two methods, analytical–numerical methods when applied to inhomogeneous bodies do not set any limitations on the relative thickness or rigidity of the coating. Here, numerical procedures are applied only at the final stage of solution. These procedures are based on Fourier or Hankel integral transformations. The accuracy of transform numerical inversion is a weak point of these methods [14]. Nevertheless they are finding application, e.g., in simulating the accumulation of contact damage in a domain between loosely coupled layers [15] and the evolution of the wheel and rail profiles [16].

The aim of this study was to elucidate the mechanical stress field distributions in a high-speed steel coating at different instants of time after the end of plasma surfacing.

2. PROBLEM DEFINITION AND SOLUTION METHODS

Let us consider the stress and strain evolution in a 0.9-cm-thick R2M9 high-speed steel layer surfaced on a1.8-cm-thick 30KhGSA steel substrate. The domain of computation is schematically shown in Fig. 1. The temperature of the layer is taken to be equal to the steel melting point, 1573 K, and that of the substrate is set equal to 293 K. It is assumed that we are dealing with plane-strain deformation.

The equation of dynamic thermoelasticity for the coating and substrate is given by

$$\rho_n \frac{\partial^2 \vec{u}_n}{\partial t^2} = \frac{\partial \sigma_{ij}^n}{\partial x_j},$$
$$c_{pn}\rho_n \frac{\partial T_n}{\partial t} = \nabla(k_n \nabla T_n) + (3\lambda_n + 2\mu_n)\alpha_{Tn} T_{0n} \frac{\partial \theta_n}{\partial t}. \quad (1)$$

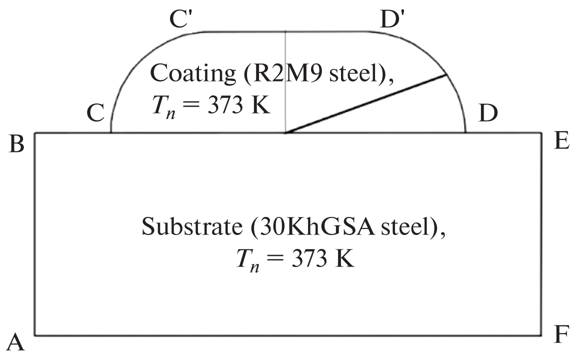

Fig. 1. On the problem of stress calculation in the deposited layer. Lines show the directions of stress distribution calculation.

Here, $\vec{u}_n$ is the displacement vector; σ_{ij}^n are stress tensor components,;c_{pn} is the specific heat; ρ_n is the density; T_n and T_{0n} are the current and initial temperatures, respectively; λ_n and μ_n are the Lame ∇ coefficients; α_{Tn} is the linear thermal expansion coefficient; θ_n is the volume strain; k_n is the thermal conductivity; ∇ is the nabla operator; and n is the number of layer.

Stress–strain coupling has the form

$$\sigma_{ij}^n = \lambda_n \theta_n \delta_{ij} + 2\mu_n \varepsilon_{ij}^n - (2\lambda_n + 2\mu_n)\alpha_{Tn}(T_n - T_{n0}), \quad (2)$$

where δ_{ij} is he Kronecker delta, $\varepsilon_{ij}^n = \frac{1}{2}\left(\frac{\partial u_{ni}}{\partial x_j} + \frac{\partial u_{nj}}{\partial x_i}\right)$ is the strain tensor, and $\theta = \varepsilon_{xx} + \varepsilon_{yy}$.

Boundary conditions for Eqs. (1) and (2) are given in Table 1.

The above set of equations was solved by the finite-element method using the Comsol Multiphysics software suite. A triangular grid with an element minimal size of 0.2 μm was applied. The elastic–plastic transition was determined by the von Mises criterion

$$\sqrt{(\sigma_{xx} - \sigma_{yy})^2 + 4\tau_{xy}} \le \sigma_y, \quad (3)$$

where σ_{xx} and σ_{yy} are the normal components of the stress tensor, τ_{xy} is the tangential component, and σ_y is the yield strength.

Table 1. Boundary conditions (see Fig. 1)

Boundary	T, q	$\sigma, \vec{u}$
AF	$-\vec{\nu} \cdot \vec{q} = 0$	$\vec{u} = 0$
AB, CC'D'D, DE, EF	$-\vec{\nu} \cdot \vec{q} = a\sigma_T\left(T_{ext}^4 - T^4\right)$, $-\vec{\nu} \cdot \vec{q} = \kappa(T_{ext} - T)$	–
CD	–	–

$\vec{\nu}$ is the normal vector, $\vec{q}$ is the heat flux density vector, σ is the mechanical stress, $\vec{u}$ is the displacement vector, κ is the heat transfer coefficient, a is the absorption factor, σ_T is the Stefan–Boltzmann constant, T is the surface temperature, and T_{ext} is the external temperature.

Table 2. Physical parameters of the coating and substrate

Parameter	Substrate (30 KhGSA steel)	Coating (R2M9 steel)
Density ρ, kg/m^3	7850	8800
Модуль Юнга E, ГПа	215	181
Linear expansion coefficient α_T, $\times 10^{-6}$ K^{-1}	117	11
Specific heat c_p, J/(kg K)	496	500
Thermal conductivity k, W/(m K)	38	27
Poisson's ratio ν	0.28	0.28
Initial temperature T_0, K	293	1573

The physical properties of the coating and substrate ate listed in Table 2. The temperature dependences of the density, specific heat, thermal conductivity, linear thermal expansion coefficient, and elasticity (Young's) modulus were obtained by approximating relevant handbook data [17, 18] included in the Comsol Multiphysics software. In Table 2 the values of these parameters are presented for initial temperatures of the coating and substrate.

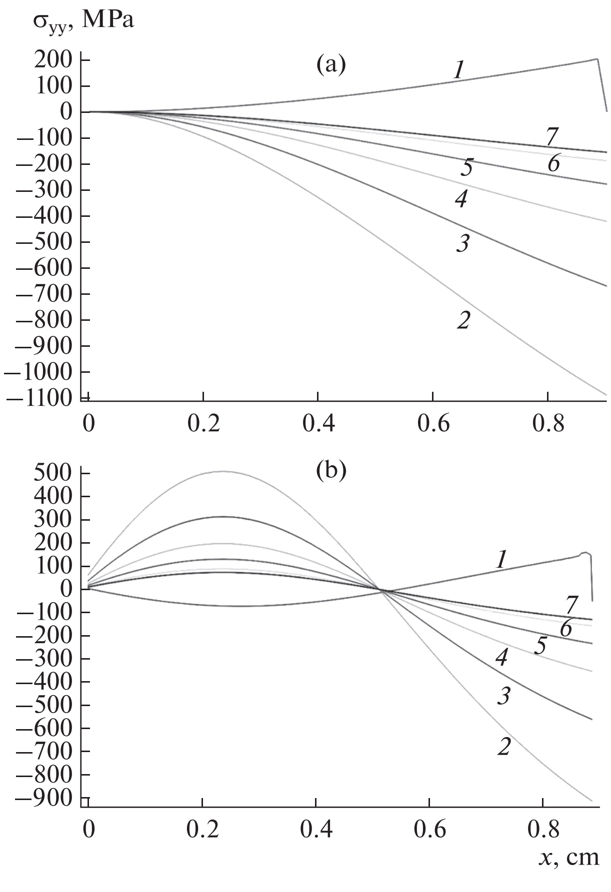

Fig. 2. Distribution of stress tensor normal component σ_{yy} in the deposited coating along (a) the central axis and (b) rounding radius at different instants of time: (*1*) 0, (*2*) 10, (*3*) 1000, (*4*) 2000, (*5*) 3000, (*6*) 4000, and (*7*) 4650 s.

3. RESULTS, DISCUSSION, AND MODEL VERIFICATION

Figure 2 shows the distribution of stress tensor normal component σ_{yy} with distance x from the coating surface. The distance was measured along the rounding radius and central axis at different instants of time. Along the central axis, normal stresses initially rise monotonically to 200 MPa at $x = 0.9$ cm. Then, tensile stresses change to compressive ones, which is in agreement with the generally accepted understanding of the material behavior under cooling.

In the case of the stress distribution along the rounding radius, the pattern is somewhat different (Fig. 2b). While initially (up to $x = 0.5$ cm) compressive stresses prevail, at further cooling tensile stresses become dominating. The latter vary nonmonotonically: their maximum shifts from $x = 0.19$ cm to $x = 0.21$ cm.

Stress tensor component σ_{xx} varies in a similar way with the only difference that stresses vary nonmonotonically over the rounding radius of the coating (Fig. 3).

Such a variation of mechanical stresses under cooling is explained by the fact that surface layers cool down faster than the rest of the coating volume [20]. Temperature field calculations showed that the thermal front propagates from the coating toward the substrate with cooling time (Fig. 4). As the front moves, it heats up secondary phase inclusions encountered in its path. They decompose because of temperature instability arising due to a linear thermal expansion coefficient mismatch between inclusions and the matrix [21].

Since the yield strength of the material grows under cooling, it might be expected that the interior of the coating is more ductile than its surface layers. To verify the model, we examined the structure and mechanical properties of the deposited layer using a KYKY-EM 6900 scanning electron microscope and an HVS-1000 hardness meter (an indentation load of 1 N). It was found that microhardness *HV* of the deposited layer (Fig. 5a) does drop from 75 to 60 GPa with distance from the surface. The nonmonotonic variation of the microhardness at depths within 4.5–6.0 mm results from the presence of carbide phase inclusions Me_6C, MeC, and Me_2C_6 (Me = Cr, Mo, V, W, Fe, Mn) and a carbide network (Fig. 5b).

The von Mises stress intensity monotonically grows with distance from the surface (Fig. 6), peaking at the coating–substrate interface irrespective of whether the stress distribution is taken along the rounding radius or along the central axis. At the end of cooling, its value in both directions roughly equals 900 MPa, which is higher than the yield strength of R2M9 steel (≈630 MPa) by a factor of 1.4. The rise in the Mises stress intensity may explain the decline of the microhardness toward the coating boundary (Fig. 5a). This supports the adequacy of the temperature model suggested.

It was noted above that temperature fields and thermoelastic stresses influence carbide phase inclusions, causing their decomposition. In [20, 21], instability criteria for a round inclusion subjected to a static compressive load were derived using the method of dynamic stability analysis of plates under the assumption that the inclusion has the form of a hingedly supported plate:

$$P_{\mathrm{cr}} = \beta_{m,n}^2 \frac{D}{R^2 h}. \quad (4)$$

In the case of a clamped plate, the expression takes the form

$$p_{\mathrm{cr}} = \alpha_{m,n}^2 \frac{D}{R^2 h}. \quad (5)$$

Here, $D = \dfrac{Eh^3}{12(1-\nu)}$, where E and ν are, respectively, the elasticity modulus and Poisson's ratio of the inclusion; R and h are, respectively, the radius and thickness of the inclusion; $\alpha_{m,\,n} = \dfrac{\pi}{4}(2m + 4n + 1)$ and $\beta_{m,n} = \pi\left(2n + m + \dfrac{3}{4}\right)$ are coefficients determined from the conditions $J_{n+1}(\alpha_{n+1,m}) = 0$ and $(\beta_{n,\,m})J_n(\beta_{n,\,m}) - (1-\nu)J_{n+1}(\beta_{n,\,m}) = 0$; $J_{n+1}(x)$ is the Bessel function; m is a constant; and n is the order of the Bessel function.

Results of calculations by formulas (4) an (5) show that for an h = 1 μm-thick chromium carbide inclusion (E = 369 GPa, ν = 0.2, $\alpha_T = 10^{-5}$ K^{-1}) with radius R = 10 μm, the critical stress is p_{cr} = 1.84 GPa in the case of a hingedly supported plate and 6.45 GPa in the case of a clamped plate. For an iron carbide inclusion (E = 292 GPa, ν = 0.3, $\alpha_T = 10^{-5}$ K^{-1}) with the same geometrical parameters, p_{cr} = 1.46 GPa in the first case and 5.10 GPa in the second case.

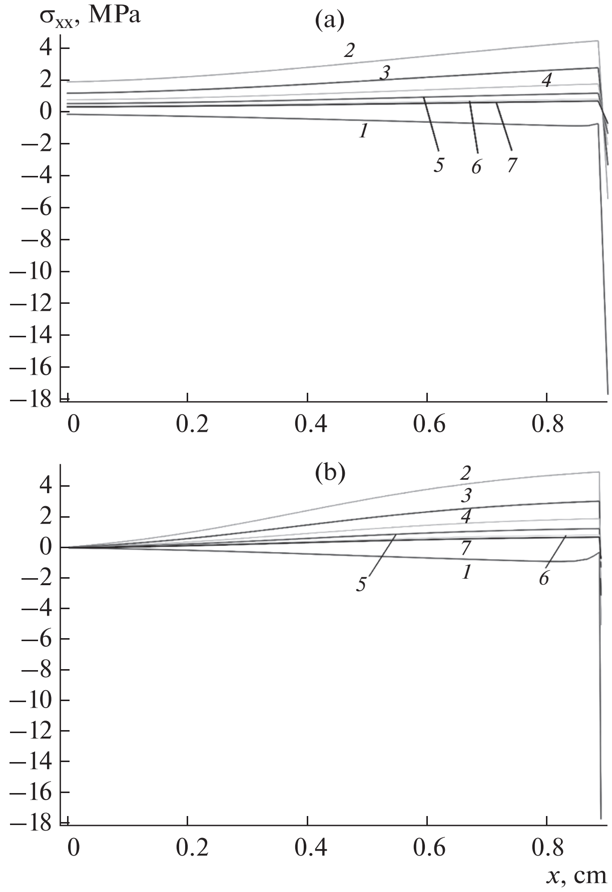

Fig. 3. Distribution of stress tensor normal component σ_{xx} in the deposited coating along the (a) central axis and (b) rounding radius at different instants of time: (*1*) 0, (*2*) 10, (*3*) 1000, (*4*) 2000, (*5*) 3000, (*6*) 4000, and (*7*) 4650 s.

In [24], a formula for stress estimation around an inclusion is presented:

$$\sigma_{\mathrm{b}} = \frac{B_1 B_2 (1+\nu_1) T_{\mathrm{m}}((\alpha_{T1} - \alpha_{T2})\nu_2 - (\alpha_{T1} + \alpha_{T2}))}{B_1(\nu_1 + 1) + B_2(1-\nu_2)}, \quad (6)$$

where $B_n = E_n/(1-\nu)$ (n = 1 or 2 for inclusion and matrix, respectively) and T_{m} is the temperature of the matrix.

From (5) it follows that for chromium carbide and iron carbide at 473 K (the temperature of martensitic transition in the matrix), σ_{b} = –2.39 and –2.31 GPa, respectively. This allows for the conclusion that inclusions 10 μm or more across and 1 μm or less thick are

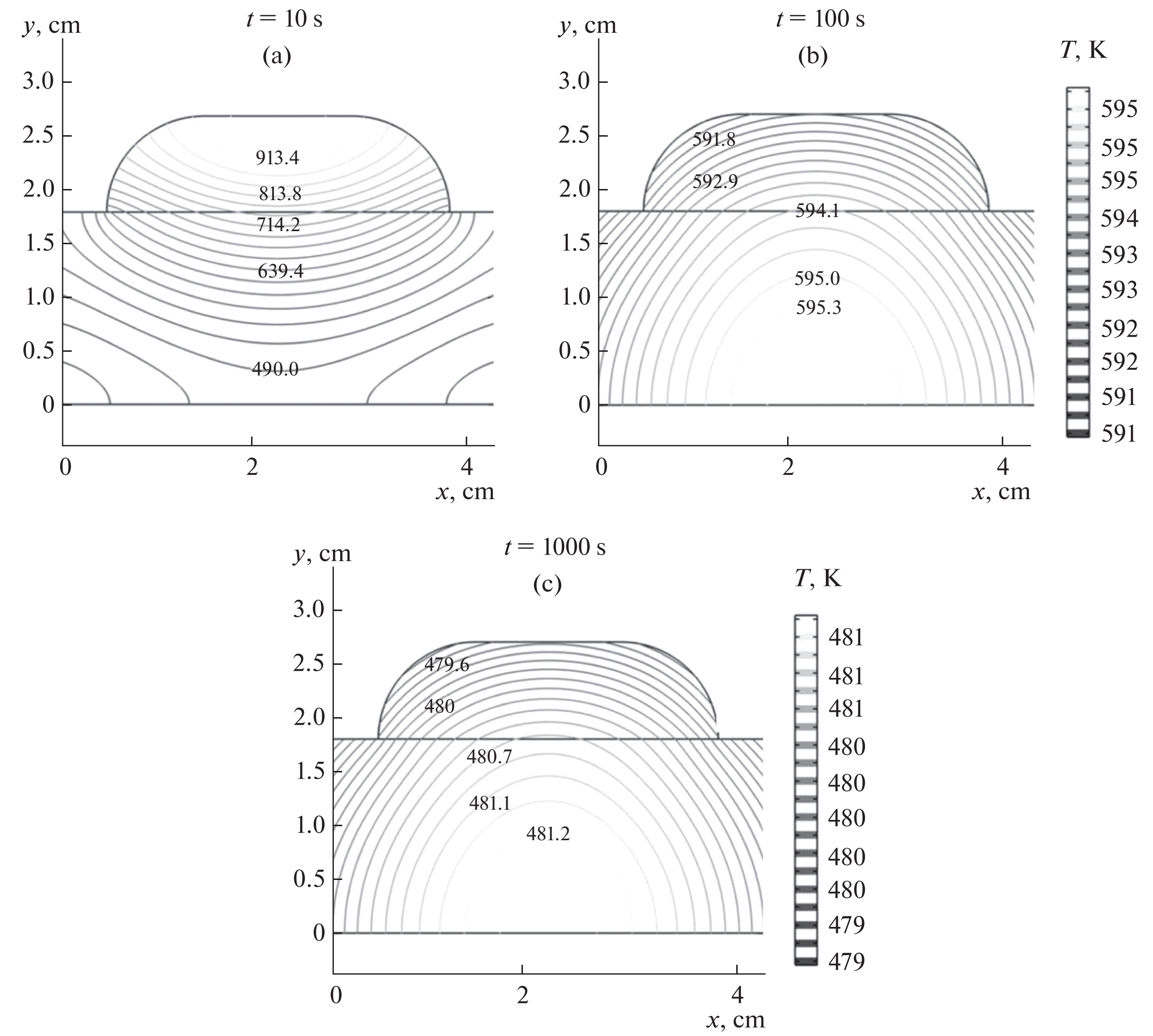

Fig. 4. Temperature fields in the coating and substrate at different instants of time: (a) 10, (b) 100, and (c) 1000 s.

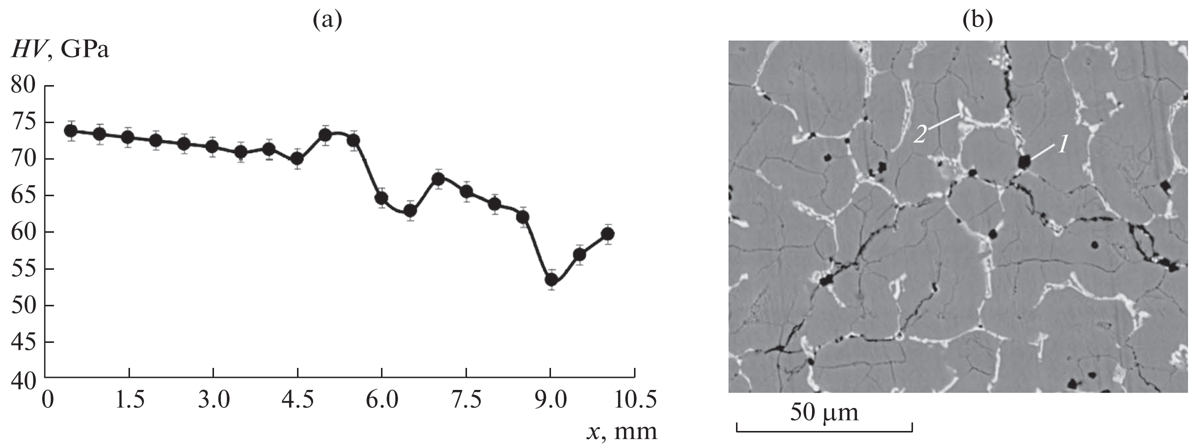

Fig. 5. (a) Microhardness distribution over the R2M9 steel coating thickness and (b) the electron microscopic image of the carbide phase: (*1*) carbide of the Me_yC_y type and (*2*) carbide network.

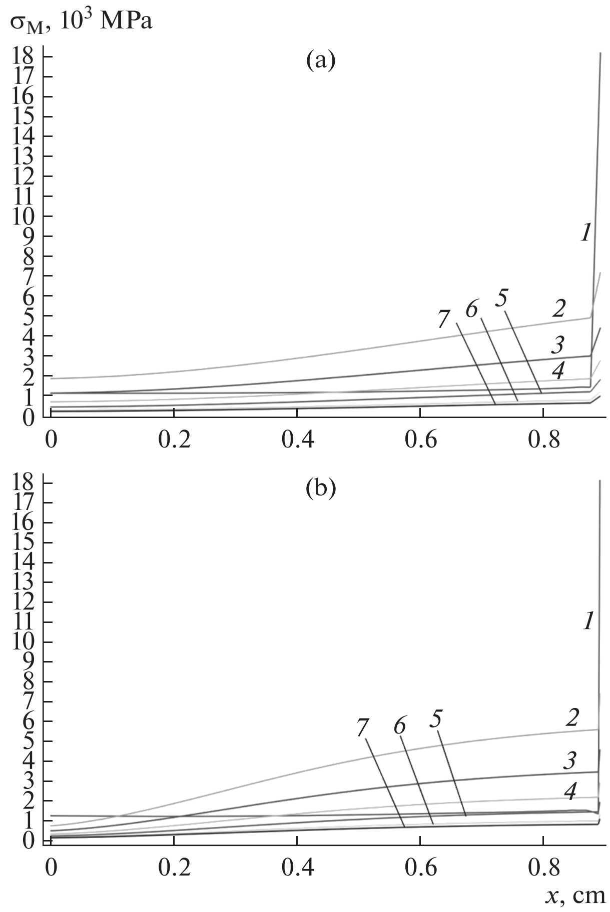

Fig. 6. Distribution of Mises stress intensity σ_M in the deposited coating along the (a) central axis and (b) rounding radius at different instants of time: (*1*) 0, (*2*) 10, (*3*) 1000, (*4*) 2000, (*5*) 3000, (*6*) 4000, and (*7*) 4500 s.

unstable and decompose, giving rise to the formation of the carbide phase.

4. CONCLUSIONS

(i) The distributions of the stress tensor normal components and von Mises stress intensity in a high-speed R2M19 steel coating on a 30KhGSA steel substrate were obtained using the finite-element method. They were taken in two directions, along the central axis and along the rounding radius of the coating, at different instants of time after the end of coating deposition.

(ii) Along the central axis, normal component σ_{yy} of the stress tensor varies monotonically toward the boundary of the coating. Along the rounding radius, σ_{yy} varies nonmonotonically and exhibits a maximum within 0.5 cm from the surface. Stress tensor component σ_{xx} and von Mises stress intensity rise monotonically along both the central axis and rounding radius.

(iii) Tensile stresses reach a maximum of 500 MPa within 10 s after the end of deposition and drop to 100 MPa in 4500 s. With time, the maximum of tensile stresses shifts into the coating.

(iv) The stability of carbide inclusions subjected to thermoelastic stresses was studied by applying methods from the theory of plates and shells. It turned out that for a chromium carbide round inclusion 10 μm in radius and 1 μm thick, critical stress p_{cr} equals 1.84 GPa when the inclusion represents a hingedly supported plate and 6.45 GPa in the case of a clamped plate. For an iron carbide inclusion with the same geometrical parameters, p_{cr} = 1.46 GPa in the model of hingedly supported plate and 5.10 GPa in the clamped plate model.

(v) Thermoelastic stresses around chromium carbide and iron carbide inclusions about 10 μm in size equal 2.3–2.4 GPa, which points to the instability of inclusions 10 ν or greater in size.

ABBREVIATIONS AND NOTATION

σ_{yy}	normal component of the stress tensor
f_1	column vector of the first layer
f_n	column vector of the *n*th layer
G_i	interlayer transfer matrix
$\vec{u}_n$	displacement vector
σ_{ij}^n	stress tensor components
σ_M	Mises stress intensity
c_{pn}	specific heat
ρ_n	density
T_n and T_{0n}	current and initial temperatures, respectively
λ_n and μ_n	Lame ∇ coefficients
α_{Tn}	linear thermal expansion coefficient
θ_n	volume strain
k_n	thermal conductivity
∇	nabla operator
n	number of layer and the order of the Bessel function
δ_{ij}	Kronecker delta
ε_{ij}^n	strain tensor
$\theta = \varepsilon_{xx} + \varepsilon_{yy}$	
σ_{xx}, σ_{yy}	normal components of the stress tensor
τ_{xy}	tangential component of the stress tensor
σ_y	yield strength

x	distance from the coating surface
HV	microhardness of the coating
E, ν	elasticity modulus and Poisson's ratio of the inclusion, respectively
R, h	radius and thickness of the inclusion, respectively
$\alpha_{m,\,n}$ and $\beta_{m,\,n}$	coefficients
$J_n + 1(x)$	Bessel function
m	constant
p_{cr}	critical stress
T_{m}	temperature of the matrix
σ_{b}	stress field around inclusion
$\vec{\nu}$	normal vector
$\vec{q}$	heat flux density vector
$\vec{u}$	displacement vector
κ	heat transfer coefficient
a	absorption factor
σ_{T}	Stefan–Boltzmann constant
T	surface temperature
T_{ex}	external temperature
c_{p}	specific heat

FUNDING

This study was supported by the Russian Science Foundation, grant no. 23-19-00186. Site ~~http://rscf.ru/project/23-19-00186~~.

CONFLICT OF INTEREST

The authors of this work declare that they have no conflicts of interest.

REFERENCES

1. N. U. Rahman, M. B. de Rooij, D. T. A. Matthews, G. Walmag, M. Sinnaeve, and G. R. B. E. Römer, "Wear characterization of multilayer laser cladded high speed steels," Tribology Int. **130**, 52–62 (2019).
2. Y. Li, Y. Wang, J. Niu, S. Liu, Y. Lin, N. Liu, J. Ma, Z. Zhang, and J. Wang, "Microstructure and mechanical properties of M2 high speed steel produced by electron beam melting," Mater. Sci. Eng., A **862**, 144327 (2023).
3. H. T. Cao, X. P. Dong, Z. Pan, X. W. Wu, Q. W. Huang, and Y. T. Pei, "Surface alloying of high-vanadium high-speed steel on ductile iron using plasma transferred arc technique: microstructure and wear properties," Mater. Design. **100**, 223–234 (2016).
4. D. O. Mul, E. G. Bushueva, D. V. Lazurenko, E. A. Lozhkina, and E. V. Domarov, "Structure and tribological properties of "carbon steel–VC containing coating" compositions formed by non-vacuum electron-beam surfacing of vanadium-containing powder mixtures," Surf. Coat. Technol. **474**, 130107 (2023).
5. G.-W. Park, S. Shin, J.-Y. Kim, Y.-M. Koo, W. Lee, K.-A. Lee, S. S. Park, and J. B. Jeon, "Analysis of solidification microstructure and cracking mechanism of a matrix high-speed steel deposited using directed-energy deposition, J. Alloys Compd. **907**, 64523 (2022).
6. N. N. Malushin, D. A. Romanov, A. P. Kovalev, V. L. Ostrovskii, and L. P. Bashchenko, "Structural-phase state of a heat-resistant high-hardness alloy formed by plasma surfacing in a nitrogen atmosphere and high-temperature tempering," Izv. Vyssh. Uchebn. Zaved., Fiz. **62** (10), 106–111 (2019).
7. H. Altenbach, G. Bruno, V. A. Eremeyev, M. Yu. Gutkin, and W. H. Müller, *Mechanics of Heterogeneous Materials* (Springer Cham, Basel, 2023).
8. N. I. Martynov, "Integral equations of plane static boundary value problems of the elasticity theory for an inhomogeneous anisotropic medium," Mech. Solids **51**, 451–471 (2016).
9. A. S. Vasiliev, S. S. Volkov, E. V. Sadyrin, and S. M. Aizikovich, "Simplified analytical solution of the contact problem on indentation of a coated half-space by a conical punch," Mathematics **8** (6), 983 (2020).
10. L. A. Molotkov, *Matrix Method in the Theory of Wave Propagation in Layered Elastic and Liquid Media* (Nauka, Moscow, 1984).
11. Yu. A. Shevlyakov, *Matrix Algorithms in the Theory of Elasticity of Inhomogeneous Media* (Vishcha Shkola, Kiev, 1977).
12. K. Holmberg, A. Laukkanen, A. Ghabchi, M. Rombouts, E. Turunen, R. Waudby, T. Suhonen, K. Valtonen, and E. Sarlin, "Computational modeling based wear resistance analysis of thick composite coatings," Tribol. Int. **72**, 13–30 (2014).
13. V. Sakalo, A. Sakalo, A. Rodikov, and S. Tomashevskiy, "Computer modeling of processes of wear and accumulation of rolling contact fatigue damage in railway wheels using combined criterion," Wear 422–423, 102900 (2019).
14. V. M. Aleksandrov and D. A. Pozharskii, *Nonclassical Spatial Problems of the Mechanics of Contact Interactions of Elastic Bodies* (Faktorial, Moscow, 1998).
15. E. V. Torskaya, "Modeling the accumulation of contact fatigue damage in the two-layer half-space for incomplete adhesion of layers," Izv. Ross. Akad. Nauk, Ser. Mekh. Tverd. Tela, No. 6, 122–130 (2011).
16. I. G. Goryacheva, S. M. Zakharov, A. P. Krasnov, A. S. Yudin, E. V. Torskaya, D. P. Markov, and I. A. Zharov, "Evaluation of the working conditions and the required properties of friction modifiers for the rolling surface of the wheel–rail system," Trenie Iznos **34** (6), 547–553 (2014).
17. *Tables of Physical Quantities: A Handbook,* Ed. by I. K. Kikoin (Atomizdat, Moscow, 1976).
18. *Steel and Alloy Grade Guide*, Ed. by A. S. Zubchenko (Mashinostroenie, Moscow, 2003).

19. R. B. Hetnarski, *Encyclopedia of Thermal Stresses* (Springer, Dordrecht, 2014).

20. P. A. Lyukshin, B. A. Lyukshin, N. Yu. Matolygina, and S. V. Panin, "Loss of stability and detachment of a thermal barrier coating from the substrate during temperature loading," Fiz. Mezomekh. **23** (5), 69–84 (2020).

21. X. Liu, B. Beausir, Y. Zhang, and W. Gan, "Heat-treatment induced defect formation in a-Al matrix in Sr-modified eutectic Al–Si alloy," J. Alloys Compd. **730**, 208–218 (2018).

22. V. D. Klyushnikov, *Lectures on the Stability of Deformable Systems* (Izd. MGU, Moscow, 1986).

23. M. R. Eslami, R. B. Hetnarski, J. Ignaczak, N. Noda, N. Sumi, and Y. Tanigawa, *Theory of Elasticity and Thermal Stresses* (Springer, Berlin, 2013).

24. V. Sarychev, S. Nevskii, S. Konovalov, A. Granovskii, and V. Gromov, "Disintegration mechanism of second phase particles under electron beams," Mater. Res. Express **6**, 106556 (2019).

Translated by V. Isaakyan

SPELL: 1. ok

9:45 87 %

scimagojr.com/jo

Russian Metallurgy (Metally)

COUNTRY

United States

Universities and research institutions in United States

Media Ranking in United States

SUBJECT AREA AND CATEGORY

9:47 87 %

scimagojr.com/jo

Quartiles

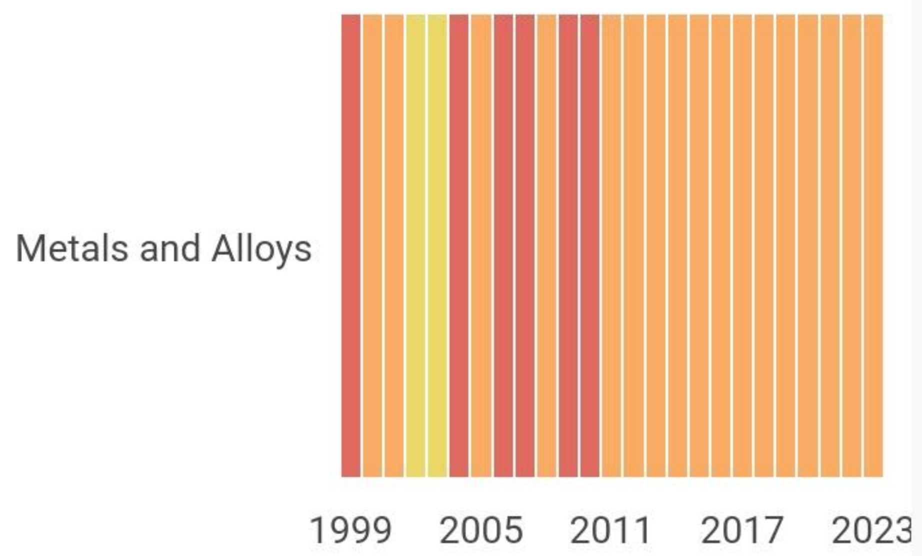

FIND SIMILAR JOURNALS ? options

1
Frontier Materials and Technologies
RUS

52%